

High-Temperature Corrosion of EB-PVD Yttria Partially Stabilized Zirconia Thermal Barrier Coatings with an Artificial Volcanic Ash Overlay

Peter Mechnich,[†] Wolfgang Braue, and Uwe Schulz

German Aerospace Center (DLR), Institute of Materials Research, 51170 Cologne, Germany

High-temperature interaction of sol-gel-derived artificial volcanic ash (AVA) matching the bulk composition of the April 15, 2010 Eyjafjallajökull (Iceland) volcanic eruption with a standard 4 mol% (7 wt%) Y_2O_3 -stabilized ZrO_2 (YSZ) electron-beam physical vapor deposition (EB-PVD) thermal barrier coating and a corresponding YSZ powder is investigated in order to access possible implications of similar volcanic ashes on the performance of coated turbine engine airfoils. Up to 900°C, AVA deposits and EB-PVD YSZ do not show significant interaction. Viscous flow above the glass transition of AVA ($T_g \sim 930^\circ C$) yields preceding wetting of EB-PVD YSZ coatings. At 1100°C, the YSZ surface is covered by a dense glaze-like AVA overlay. At 1200°C, AVA is mostly infiltrating the coating, leaving a crystalline plagioclase- and hematite-type residue at the interface. Moreover, some $ZrSiO_4$ is formed at the expense of YSZ. The overall thermochemical effects on short-term exposure of the EB-PVD YSZ coating to a small AVA load were moderate, in particular before complete infiltration. On the other hand, AVA acts as a solvent for the stabilizing Y_2O_3 beyond 1000°C and a progressive depletion of Y_2O_3 in the YSZ is observed at the AVA/YSZ interface. Detrimental effects on YSZ phase stability and hence coating lifetime cannot be ruled out for long-term exposure and higher AVA loads.

I. Introduction

Y_2O_3 partially stabilized ZrO_2 (YSZ) is the state-of-the-art material for thermal barrier coatings (TBCs) of turbine engine airfoils.¹ The solid solution with 4 mol% Y_2O_3 stabilizes the tetragonal crystal structure on cooling, thus preventing the detrimental volume change related to the phase transformation of the high-temperature tetragonal structure to the low-temperature monoclinic structure of pure ZrO_2 . YSZ TBCs for aircraft engines are usually fabricated by electron-beam physical vapor deposition (EB-PVD), which produces a characteristic columnar and highly porous microstructure showing beneficial strain tolerance and low thermal conductivity. Since the early 1990s, a special type of degradation observed in hot sections of turbine engines has gained increasing attention. This phenomenon is related to airborne inorganic dust particles that are ingested by the turbine, melted in the combustion zone, and subsequently are deposited on hot surfaces.^{2–7} The chemical composition of airborne particles typically reflects the bulk chemical composition of sediments and dusts; thus, the dominating oxides are SiO_2 , Al_2O_3 , CaO , and MgO . Consequently, this kind of degradation commonly is referred to as calcia–magnesia–alumina–silica (CMAS type) hot corrosion. Probably, the most prominent and technologically relevant example is the CMAS-type degradation of EB-PVD YSZ-coated airfoils of aero engines. De-

pending on the airfoil surface temperature, liquefied CMAS is even able to penetrate the columnar YSZ coating, hence producing mechanical stresses on thermal cycling and significantly reduced lifetime. Moreover, the thermal barrier function of EB-PVD YSZ may be deteriorated by infiltration of porosity. The thermochemical behavior of EB-PVD YSZ coatings with artificial silica-rich CMAS-type deposits has been examined extensively.^{8,9} On the other hand, CMAS-type deposits with a much lower lime-to-silica ratio and also containing significant amounts of Fe_2O_3 and TiO_2 were reported from an in-service high-pressure turbine airfoil.¹⁰ The presence of Fe_2O_3 at the YSZ/CMAS reactive interface was found to induce the formation of complex, Ca, Zr-garnets of the kimzeyite type.¹¹ In spring 2010, the plume of the massive eruption of the Eyjafjallajökull volcano in southern Iceland and the following discussion on possible detrimental effects of its ashes on the performance and safety of aero engines imposed serious limitations on European air traffic. According to the chemical analyses published online¹² in the aftermath of the April 15, 2010 eruption, Eyjafjallajökull volcanic ash exhibits a much higher SiO_2 content and chemical complexity compared with the CMAS-type deposits reported in literature (Table I). A key feature is also the much lower content of alkaline earth oxides (CaO , MgO) and, on the other hand, a significant content of alkaline oxides with Na_2O dominating K_2O . In the total alkali versus silica diagram¹³, the April 15, 2010 ash composition plots into the regime of trachyandesite-type volcanic rocks characterized by intermediate silica content. In the recalculation of the bulk analysis to a normative mineral assemblage,¹⁴ plagioclase solid solution dominates over feldspar $KAlSi_3O_8$ and very little free SiO_2 (quartz) along with pyroxene and minor additional phases. It must be emphasized that volcanic ashes are rapidly quenched frequently and therefore consist of glassy phases with only minor crystalline components.

In the present work, we report preliminary results on the compatibility between standard 4 mol% YSZ EB-PVD TBCs (and corresponding YSZ powders, respectively) in the presence of sol-gel-derived artificial volcanic ash (AVA) having a bulk composition close to the ash of the April 15, 2010 Eyjafjallajökull eruption. The thermochemical properties of AVA are analyzed. The microstructural development of the AVA/YSZ interface and newly formed phases on AVA melting and partial infiltration into the coating is monitored by analytical electron microscopy. The effects of volcanic ashes on the performance of EB-PVD YSZ TBCs in turbine engines are accessed.

II. Experimental Procedure

The starting materials for the synthesis of AVA were $Al(NO_3)_3 \cdot 9H_2O$, $Fe(NO_3)_3 \cdot 9H_2O$, $Mg(NO_3)_2 \cdot 6H_2O$, $Ca(NO_3)_2 \cdot 4H_2O$, $NaNO_3$, KNO_3 , $Mn(NO_3)_2 \cdot 4H_2O$, tetraethyl orthosilicate (TEOS), tetra-ethyl orthotitanate (TEOT), and $(NH_4)_2HPO_4$ (Merck, Darmstadt, Germany). A laboratory ball mill (Pulverisette 7 premium line, Fritsch, Idar-Oberstein,

J. Smialek—contributing editor

Manuscript No. 28205. Received June 18, 2010; approved September 1, 2010.

[†]Author to whom correspondence should be addressed. e-mail: peter.mechnich@dlr.de

Table I. Chemical Composition of Oxide Materials Related to the High-Temperature Degradation of Y₂O₃-Stabilized ZrO₂ Thermal Barrier Coating

Values in wt% (mol%) [†]	Lab-scale CMAS ^{2,3}	Example of an in-service deposit on HPT airfoil ⁴	Eyjafjallajokull volcanic ash April 15, 2010 ^{†,6}	Artificial volcano ash (this work)
SiO ₂	48.50 (48.15)	22.40	57.69	57.90 (63.05)
Al ₂ O ₃	11.80 (6.90)	10.10	15.48	15.50 (9.95)
CaO	33.20 (35.32)	33.60	5.15	5.20 (6.07)
MgO	6.50 (9.62)	9.90	2.15	2.15 (3.49)
FeO	—	15.40	9.61	9.65 (8.79)
TiO ₂	—	3.00	1.59	1.60 (1.31)
Na ₂ O	—	—	5.25	5.25 (5.54)
K ₂ O	—	—	1.72	1.75 (1.22)
MnO	—	—	0.27	0.27 (0.25)
P ₂ O ₅	—	0.7	0.73	0.73 (0.33)
Traces (S, Ni, Zr, etc.)	—	4.9	0.36	—

[†]Values in mol% are only given for synthetic materials without unspecified trace elements. [‡]Average of five analyses. CMAS, calcia–magnesia–alumina–silica.

Germany) was used for powder preparation. Powder grain size distribution was determined with a particle-size analyzer (Mastersizer 2000, Malvern Instruments, Malvern, U.K.). Approximately 250 μm thick 4 mol% YSZ TBC deposited by EB-PVD (von Ardenne Anlagentechnik, Dresden, Germany) on alumina substrates were used as test specimens. Diffusion couples were prepared by depositing about 20 mg/cm² of AVA powder on top of EB-PVD YSZ-coated coupons. Reference experiments were performed using powder mixtures of AVA and 1200°C pre-annealed 4 mol% YSZ (TZ-4Y, Tosoh Advanced Ceramics, Tokyo, Japan) in a 2 to 1 weight ratio. The tetragonal, monophase composition of the YSZ starting powder was confirmed by X-ray diffraction (XRD) analysis. All heat treatments were carried out in air in a resistor-heated chamber furnace with annealing times of 1 h, respectively. Samples were characterized by X-ray powder diffraction (XRD) (Siemens D 5000, CuK α radiation and secondary graphite monochromator, EVA/Topas 4.2 software package, Bruker AXS, Karlsruhe, Germany) and differential scanning calorimetry (DSC 404, Netzsch, Selb, Germany). A DSM Ultra 55 scanning electron microscope (SEM) (Carl Zeiss NTS, Wetzlar, Germany with Inca EDS, Oxford, Abingdon, U.K.) was used for microstructural analyses. Focused-ion-beam (FIB)-assisted analytical transmission electron microscopy (TEM) was performed in a Strata 205 FIB system and a Tecnai F30 TEM-scanning transmission electron microscope (STEM) utilizing a field-emission gun (FEI Inc., Eindhoven, the Netherlands).

III. Results and Discussion

(1) Preparation and Characterization of AVA

In order to obtain chemical homogeneity even at low processing temperature, AVA was prepared by the sol–gel technique. Based on the chemical analysis of the Eyjafjallajokull (Iceland) volcano ash,⁶ a similar composition was defined, however, excluding the trace elements (Table I, right-hand column). Deionized water (100 g) was used as solvent for the metal-nitrates Me(NO₃)_x · xH₂O. Appropriate amounts of TEOS and TEOT were premixed and then added dropwise to the aqueous solution under vigorous stirring. Finally, the calculated amount of (NH₄)₂HPO₄ was dissolved in some water and added dropwise to the precursor sol. The precursor sol was kept stirring gently in a closed beaker at ambient temperature for 48 h in order to achieve complete hydrolysis of TEOS and TEOT. Precursor gelation and evaporation of solvent were performed at RT in an open dish for another 48 h. The dried precursor flakes were annealed in a Pt crucible at 800°C and subsequently ball milled in isopropanol using HIP-Si₃N₄ milling jars and milling balls (30 min, 300 rpm, ball/powder ratio 5:1). A schematic flow-chart of the preparation of AVA is depicted in Fig. 1. After ball milling,

AVA basically exhibits a continuous grain size distribution between 0.5 and 70 μm , a maximum volume fraction at about 15 μm , and a d_{50} value of approximately 12 μm (Fig. 2). AVA is mostly X-ray amorphous as indicated by the XRD profile plotted in Fig. 3. The majority of the XRD peaks are obviously related to the hematite Fe₂O₃. Some small XRD peaks not matching the hematite pattern, however, may be assigned to two coexisting crystalline phases, pseudobrookite Fe₂TiO₅ and pyroxene-type aegirine NaFeSi₂O₆. Generally, XRD peaks are broad and weak, indicating a poor crystallinity. The inset in Fig. 3 shows an SEM image of a polished cross section of AVA after annealing at 800°C. As indicated by XRD, nanosized precipitates, presumably hematite Fe₂O₃, are embedded in a dark contrasted matrix representing the dominating amorphous part of AVA. Thermal properties of AVA were determined using DSC analysis up to 1400°C using a heating rate of 10 K/min (Fig. 4). The DSC plot reveals two major thermal effects. An endothermic phase transition is evident between approximately 900° and 950°C. The characteristic sigmoidal shape is explained with a stepwise change in heat capacity and obviously refers to the glass transition of AVA. By means of a simple graphic approach (Fig. 4, dashed lines), the glass transition temperature, T_g , is estimated to be approximately 930°C. A second significant endothermic reaction with a peak temperature of about 1300°C is easily explained by the melting of AVA. However, due to the fact that the 1300°C peak is very broad and the DSC curve shows a significant discontinuity starting even below 1200°C, obviously a melting temperature range rather than a well-defined melting point exists for AVA.

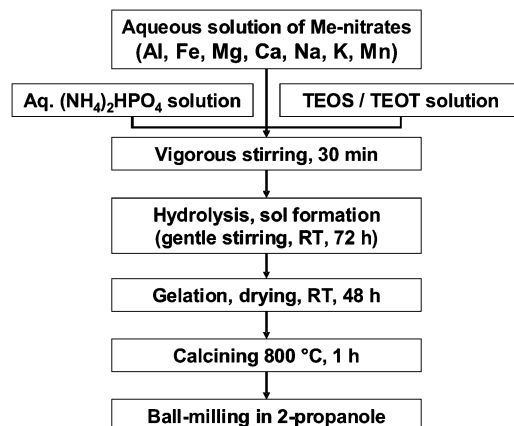


Fig. 1. Processing scheme for the synthesis of artificial volcanic ash.

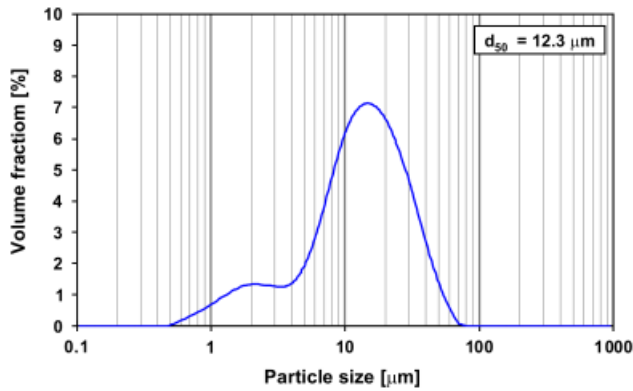


Fig. 2. Particle size distribution of sol-gel-derived artificial volcanic ash (AVA) upon ball milling.

(2) Phase Development of AVA/YSZ Powder Mixtures on Annealing Between 900° and 1200°C

A mixture of AVA (67 wt%) and TZ-4Y powders (33 wt%) was used to determine chemical reactions at high temperatures. Figure 5 shows the XRD profiles on annealing for 1 h at 900°, 1000°, 1100°, and 1200°C, respectively. At 900°C, there is no evidence for newly formed phases, i.e. the XRD profile is dominated by the YSZ powder and only small Fe₂O₃ (hematite) peaks related to AVA are detected. At 1000°C, a newly formed phase with an XRD reflection around 28° 2θ may be related to a coexisting plagioclase-type solid solution. This phase also coexists with hematite and YSZ after annealing at 1100°C. Regarding the tetragonal YSZ, a change of its XRD profile is obvious: the difference between the *d*-spacing of the (013) and (211) reflections is growing considerably, i.e. the peaks are getting more separated. Note that the YSZ reflections are indexed in the tetragonal and not in the cubic cell frequently used in the TBC literature. After annealing at 1200°C, the XRD profile has changed significantly. Besides the lower intensity of the peaks associated with a plagioclase-type phase, the formation of zircon (ZrSiO₄) is evident, which requires the partial decomposition of YSZ. The crystallization of ZrSiO₄ is noteworthy because this reaction is extremely sluggish in the binary ZrO₂-SiO₂ at 1200°C.^{15,16} However, the presence of additional oxides may accelerate significantly the ZrSiO₄ formation. Our experience shows that especially Y₂O₃ can increase reactivity. The present scenario may be explained by a sequential decomposition of YSZ, i.e. with a progressive dissolution of Y₂O₃ by AVA until ZrSiO₄ nucleates and grows at the interface between the now

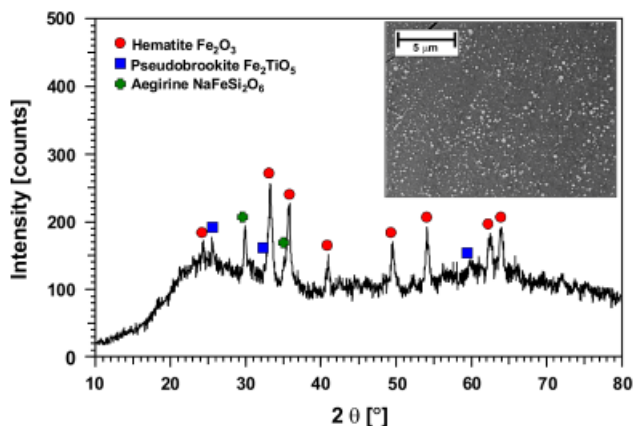


Fig. 3. X-ray diffraction profile of as-processed artificial volcanic ash. The increased background is due to the dominance of amorphous phase. Crystalline constituents include hematite Fe₂O₃ (dot symbols), pseudobrookite Fe₂TiO₅ (squares), and aegirine-type clinopyroxene NaFeSi₂O₆ (crosses).

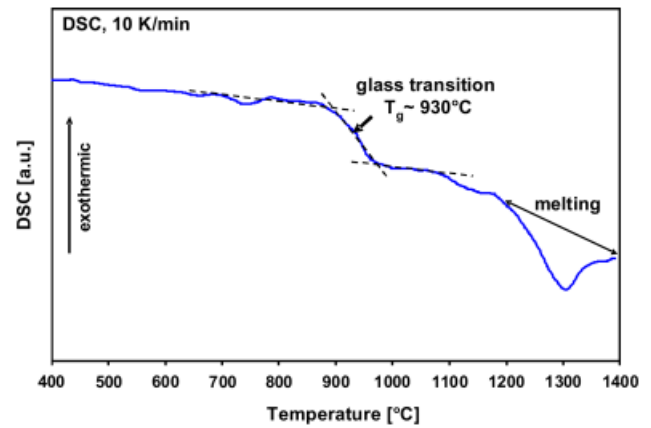


Fig. 4. Differential scanning calorimetry (DSC) of artificial volcanic ash in the 400°–1400°C temperature range. Note the sigmoidal glass transition at approximately 930°C and the melting range extending above 1180°C.

Y₂O₃-enriched amorphous phase and the residual ZrO₂. Compared with the situation at 1100°C, the peak shift of the tetragonal YSZ is further increasing, as indicated by the more pronounced splitting of (013) and (211) and an additional splitting of the (112) and (020) reflections. In order to quantify the observed YSZ peak shifts, YSZ lattice constants were determined by analytical XRD profile fitting using the tetragonal ZrO₂ structure model¹⁷ (S.G. *P4₂/nmc*, 10–80° 2θ, 0.02° steps and pseudo-Voigt peak shape function). The refined tetragonal lattice constants *a*_{tet} and *c*_{tet} of YSZ after annealing are shown in Fig. 6, respectively. Between 900° and 1000°C, values are changing only slightly. Above 1000°C, a significant decrease of *a*_{tet} from 0.3614 to 0.3604 nm is observed. Simultaneously *c*_{tet} increases from 0.5171 to 0.5179 nm at 1200°C. These results support the concept of a progressive dissolution of Y₂O₃ from YSZ by the coexisting amorphous phase. A straightforward method to derive the YSZ composition from XRD data has been elaborated by Ingel and Lewis,¹⁸ taking advantage of an almost linear relationship between the lattice constants and the Y₂O₃ content. For the tetragonal lattice constants *a*_{tet} and *c*_{tet} and a molar content Y₂O₃ between 2% and 7%, the relationships are given by the authors as *a*_{tet} × √2 = 0.5080 + 0.0698*M* / (100 + *M*) and *c*_{tet} = 0.5195 – 0.0618*M* / (100 + *M*), where *M* is mol% Y₂O₃ in YSZ. Consequently, there exists a linear relationship between *M* and the tetragonality *c*/*d*, where *d* = *a*_{tet} × √2. The calculation of *c*/*d* between *M* = 2 and 5 is

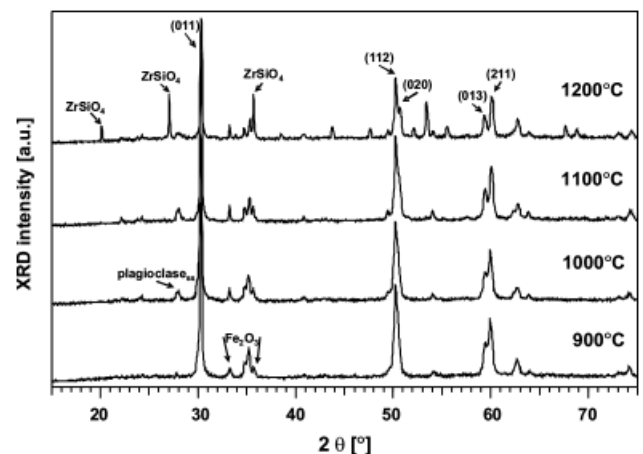


Fig. 5. X-ray diffraction (XRD) profiles showing the crystallization of artificial volcanic ash/Y₂O₃-stabilized ZrO₂ powder mixtures on 1 h annealing between 900° and 1200°C. Note ZrSiO₄ formation at 1200°C.

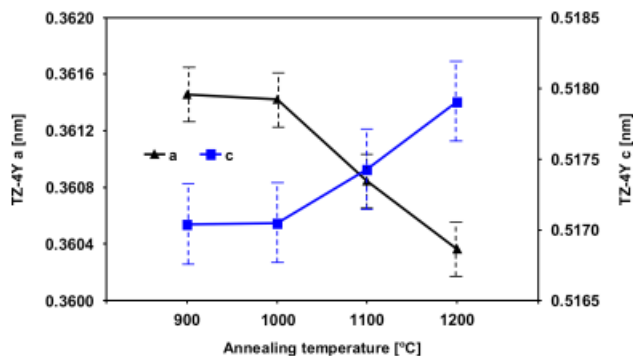


Fig. 6. Evolution of tetragonal cell parameters of the t -ZrO₂ phase in the artificial volcanic ash/Y₂O₃-stabilized ZrO₂ powder mixture on annealing between 900° and 1200°C.

plotted as a straight line in Fig. 7. The diamonds in Fig. 7 represent the c/d values derived from our lattice constants obtained for the different annealing temperatures, respectively. We obtain a value of approximately 4.5 mol% Y₂O₃ at 900°C, which obviously is higher than the expected value of 4 mol%. This may be due to the fact that the used relationships between a_{tet} , c_{tet} , and M represent an approximation of literature data and hence the calculation of M from our own refined lattice constants a_{tet} and c_{tet} is performed on a different database. Nonetheless, a significant Y₂O₃ depletion of YSZ at higher annealing temperatures is obvious. After 1 h at only 1200°C, the c/d value yields a Y₂O₃ content of approximately 2.5 mol%, meaning a relative Y₂O₃ loss of almost 50% with respect to the initial state. Despite the massive depletion of the stabilizing Y₂O₃, a phase transformation to monoclinic ZrO₂ was not observed under the present experimental conditions.

(3) Microstructural Development of AVA Deposits on YSZ-TBC on Annealing Between 900° and 1200°C

The SEM cross sections in Fig. 8 feature an overview of the microstructural development of the AVA deposited on EB-PVD YSZ on heat treatments. After annealing for 1 h at 900°C, the AVA deposit is still granular and only offers isolated contact points to the faceted EB-PVD column tips (Fig. 8(A)).

After annealing at 1000°C, the AVA deposit exhibits significant densification, obviously caused by softening and subsequent viscous flow beyond the glass transition at about 930°C (Fig. 8(B)). Consequently, the contact areas between the AVA deposit and EB-PVD YSZ are also increasing. This effect is dominant after annealing at 1100°C. At this stage, AVA does form a kind of glaze, fully enveloping the EB-PVD YSZ column

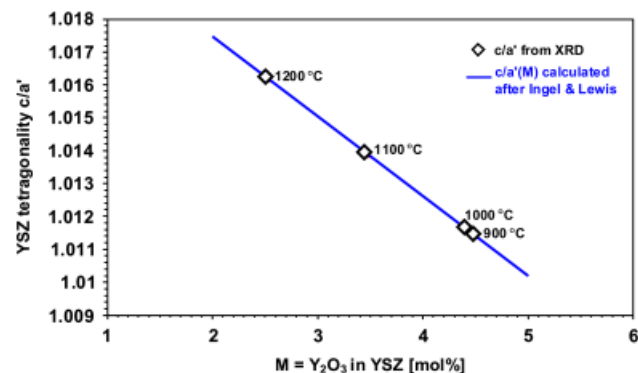


Fig. 7. Y₂O₃ depletion of the t -ZrO₂ phase in the artificial volcanic ash/Y₂O₃-stabilized ZrO₂ (YSZ) powder mixture in the 900°–1200°C temperature range as derived from refined lattice constants a and c and the Ingel and Lewis relationship (tetragonality c/d versus molar Y₂O₃ content M in YSZ), respectively.

tips. Moreover, higher magnification reveals a significant, up to 50 μ m deep penetration of AVA into the intercolumnar gaps (Fig. 8(C), dashed line). The situation completely changes at 1200°C: now, the former AVA deposit has almost completely disappeared with only some residual crystalline particles left on top of the EB-PVD YSZ column tips (Fig. 8(D)). The majority of AVA has been infiltrated into the intercolumnar pores of the YSZ coating. As indicated by the dashed line, the infiltration depth reaches approximately 150 μ m, i.e. 60% of the coating thickness. Figure 9 provides a detailed sectional view of the AVA/YSZ interface of the 900°, 1000°, and 1100°C specimens, respectively. It turns out that, independent of the degree of wetting, the characteristic feather-arm-type morphology of the EB-PVD YSZ coating is not affected by infiltration. Moreover, no significant reactions or newly formed phases are present. As observed at lower magnification, the situation changes considerably at 1200°C. At the former AVA/YSZ interface, light gray-contrasted aggregates of a second phase are clearly visible (Fig. 10(A)). EDS analysis revealed that these grains are not only Fe₂O₃ rich (80.9 mol%) but also contain 3.9 mol% Al₂O₃, 6.7 mol% MgO, and 8.5 mol% TiO₂. Therefore, it may be assumed that this phase is an Fe₂O₃-rich spinel- or hematite-type solid solution. A second, dark-contrasted phase coexists both with the Fe₂O₃-rich phase and the YSZ. EDS analyses revealed that this phase contains SiO₂ (64.9 mol%), Al₂O₃ (17.0 mol%), CaO (13.0 mol%), and Na₂O (5.1 mol%). Considering the XRD analyses, it is anticipated that this phase represents a plagioclase-type solid solution in the binary system albite (NaAlSi₃O₈)–anorthite (CaAl₂Si₂O₈). Taking into account the EDS data, the present phase approximately corresponds to an 1/1 anorthite/albite plagioclase (theoretical molar composition 62.5% SiO₂, 18.75% Al₂O₃, 12.5% CaO, and 6.25% Na₂O). Along with Fe₂O₃-rich and plagioclase solid solutions, the formation of zircon ZrSiO₄ is also observed in AVA/EB-PVD YSZ diffusion couples (Fig. 10(B)). Typically, ZrSiO₄ is located on top of intercolumnar gaps bridging individual YSZ columns. A filling of feather-arm type pores by ZrSiO₄ is also frequently observed.

In contrast to the specimen annealed at lower temperatures, the feather-arm structure of the YSZ now shows significant degradation, obviously due to grain growth and pore coalescence. Intercolumnar pores are either completely infiltrated by AVA-derived glass, or, in other locations the glass is forming isolated pockets.

The SEM analyses were corroborated by analytical TEM work comprising diffraction contrast, dark-field/Z-contrast imaging in scanning transmission (STEM) mode, energy-dispersive nanospectroscopy, and various electron diffraction techniques. The TEM data, particular from electron diffraction, allow for the unambiguous identification of the Fe₂O₃-rich solid solution; rhombohedral Ti-, Mg-, and Al-bearing hematite coexists with the plagioclase solid solution and YSZ (Fig. 11(A)). The formation of a spinel-type phase can be ruled out. The TiO₂ concentration in hematite was of the order of 9 mol% with additional amounts of MgO and Al₂O₃ totaling 11 mol% emphasizing hematite also being a sink for TiO₂ and Fe₂O₃ previously bound in pseudobrookite and aegirine in the AVA starting material (Fig. 3). As compared with the nanoscale hematite grain size in the as-processed AVA, considerable grain growth has occurred in the 1200°C state followed by hematite accumulation at the YSZ column tips. The formation of fast-growing plagioclase entrapping numerous hematite crystals (Fig. 11(A)) is indicative of the dynamic reactive AVA/YSZ interface. As shown in Fig. 11(B), growth of ZrSiO₄ proceeded from the YSZ/glass interface down the intercolumnar pore channels leaving a corrosive liquid phase that may still penetrate further into the coating. Small probe microanalysis of the glass revealed a substantial Y₂O₃ concentration along with AVA constituents. These TEM results provide additional support for the previously discussed concept of a sequential decomposition of YSZ to ZrSiO₄ at the interface between the Y₂O₃-enriched amorphous phase and residual ZrO₂ (see powder mixtures section).

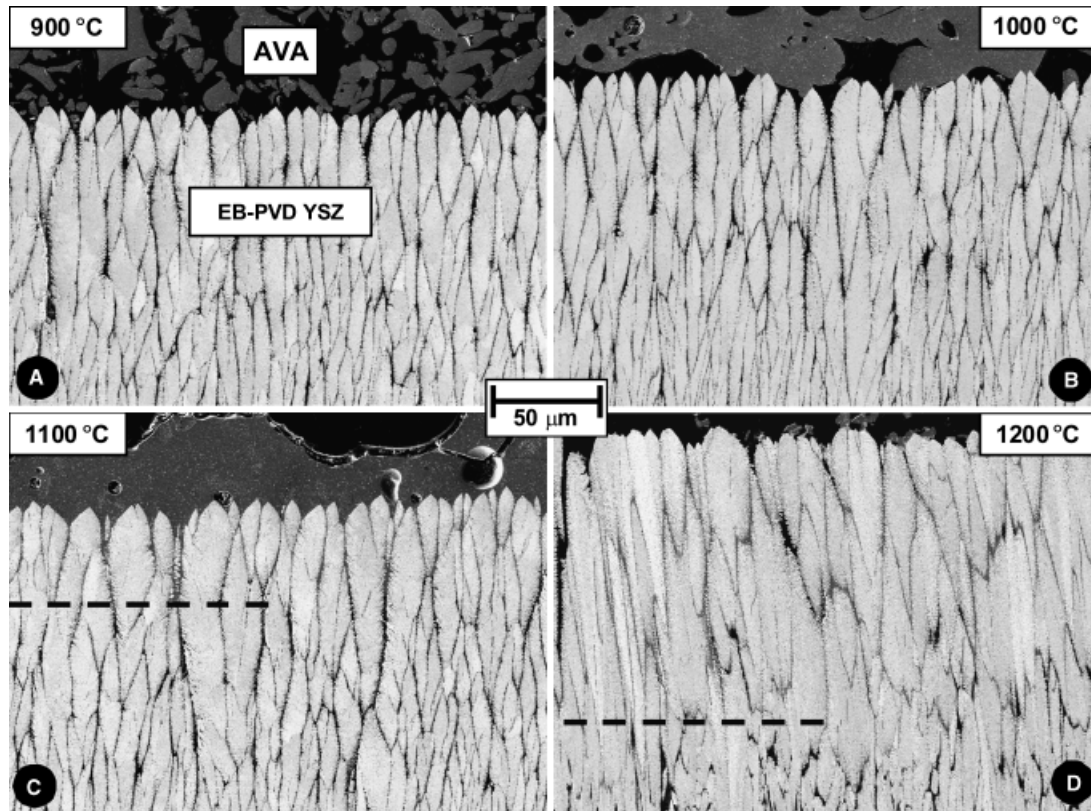


Fig. 8. The microstructural development of the artificial volcanic ash(AVA)/EB-PVD Y_2O_3 -stabilized ZrO_2 interface after 1 h annealing between 900°C (A), 1000°C (B), 1100°C (C), and 1200°C (D) (SE images). Infiltration levels of molten AVA in the coating are indicated by dashed lines.

The SEM-EDS analysis reveals a different chemical composition of the infiltrated amorphous phase and the residual deposit. Moreover, there are significant deviations in stoichiometry between (i) initial AVA and both (ii) the infiltrated amorphous phase and (iii) the residual deposit (Fig. 12). This finding and the results of the previously described DSC analysis support the idea that a partial mobilization and the subsequent

infiltration of AVA have occurred, leading to the observed Fe_2O_3 -, CaO -, and Al_2O_3 -rich deposit and correspondingly to an SiO_2 -enriched but Fe_2O_3 - and CaO -depleted liquid phase. This liquid, on the other hand, is able to dissolve a significant quantity of YSZ as indicated by the ZrO_2 and Y_2O_3 contents well above the detection limit. A small, but significant effect was observed for the alkaline oxides; the content of Na_2O is

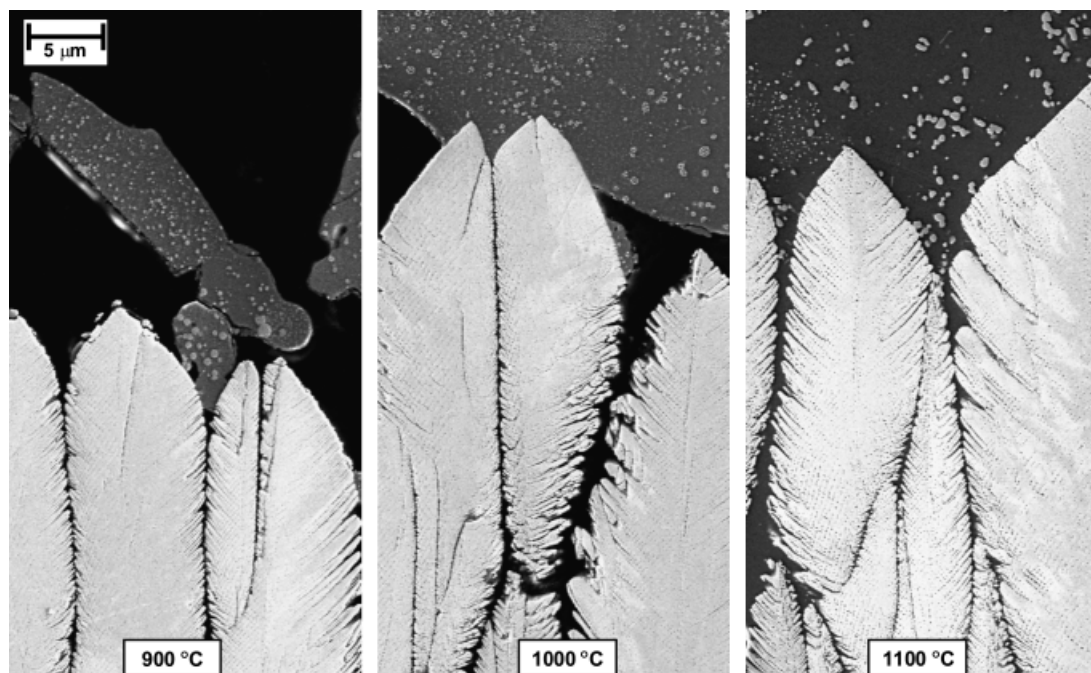


Fig. 9. High-magnification SEM images of the artificial volcanic ash/EB-PVD Y_2O_3 -stabilized ZrO_2 interface proving the lack of interfacial reactions and the retention of the characteristic feather-arm morphology in the coating upon 1 h annealing at 900°, 1000°, and 1100°C, respectively.

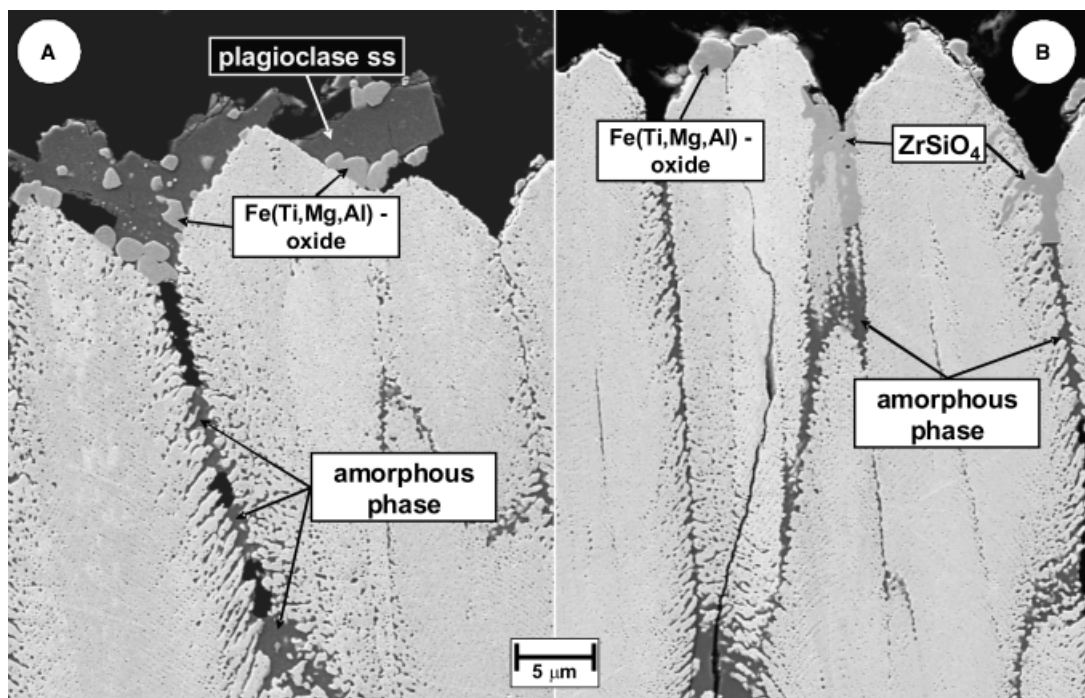


Fig. 10. High-magnification SE images of the artificial volcanic ash/EB-PVD Y_2O_3 -stabilized ZrO_2 (YSZ) interface emphasizing the onset of the interfacial reaction after 1 h at $1200^\circ C$ giving rise to the formation of a plagioclase-type solid solution (A), a re-crystallized Fe_2O_3 -rich solid solution (A and B) and $ZrSiO_4$ (B). Note that the YSZ column tips are still faceted at this stage.

decreasing at $1200^\circ C$, indicating some volatilization. Moreover, K_2O could not be detected at $1200^\circ C$, i.e. it has been completely volatilized.

The XRD results for the AVA/YSZ powder mixture raise the question whether a progressive Y_2O_3 depletion of YSZ is observed in the AVA/EB-PVD YSZ diffusion pairs as well. An accurate SEM-EDS quantification, however, is difficult due to the problematic deconvolution of overlapping Y and Zr L -peaks. However, small probe EDS analyses performed close to the AVA/EB-PVD YSZ-reactive interface indicate that the relative extent of the Y_2O_3 depletion seems to be similar to that observed in the powder mixtures: after annealing for 1 h at $1200^\circ C$, we also observed a Y_2O_3 depletion of approximately 50% with respect to the baseline value. Interestingly, the EDS

analyses gave no evidence for an uptake of the two other common stabilizing elements MgO and CaO by YSZ. Under the present conditions, the dominating driving force for the diffusion of species seems to be the concentration gradient of Y_2O_3 whereas MgO and CaO are presumably located in thermodynamically stable environments.

The wetting and infiltration behavior of AVA differ considerably from the standard CMAS-type recession reported in the literature.^{8,9} CMAS-type deposits were found to melt and subsequently infiltrate EB-PVD YSZ above 1230° – $1240^\circ C$. Generally, the onset temperature for interaction is much lower in case of AVA. The AVA deposit exhibits softening above the glass transition rather than a well-defined melting point; hence, the infiltration occurs by viscous flowing rather than by instantaneous

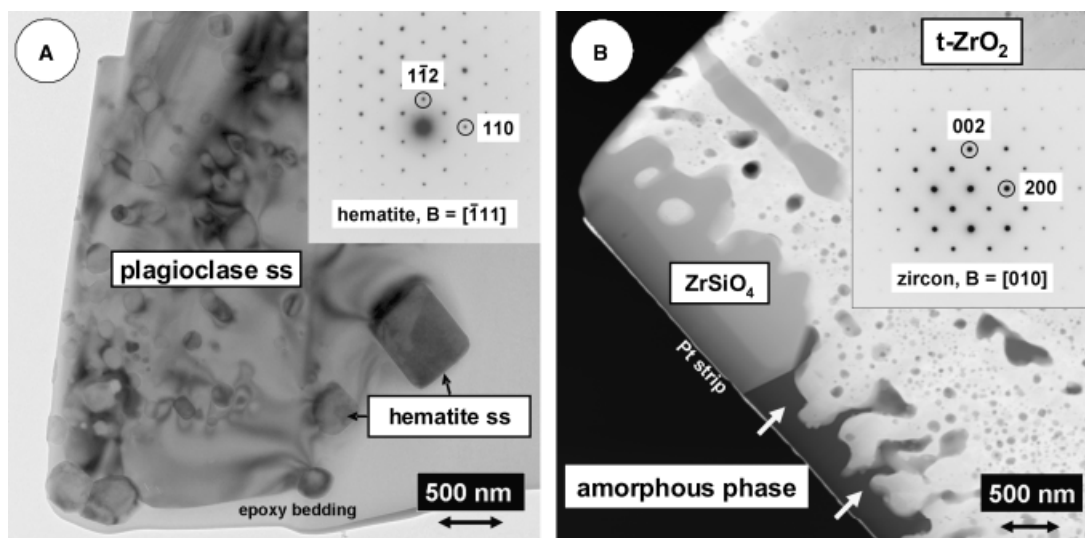


Fig. 11. (A) Bright-field transmission electron microscopy image showing newly formed plagioclase along with recrystallized Ti-bearing hematite inclusions (as confirmed by electron diffraction) at the artificial volcanic ash (AVA)/ Y_2O_3 -stabilized ZrO_2 (YSZ) reactive interface at $1200^\circ C$. (B) Dark-field scanning transmission electron microscopy image of an intercolumnar pore channel just below the AVA/YSZ interface revealing zircon $ZrSiO_4$ (as confirmed by electron diffraction) and the Y_2O_3 -bearing aluminosilicate amorphous phase penetrating further into the coating.

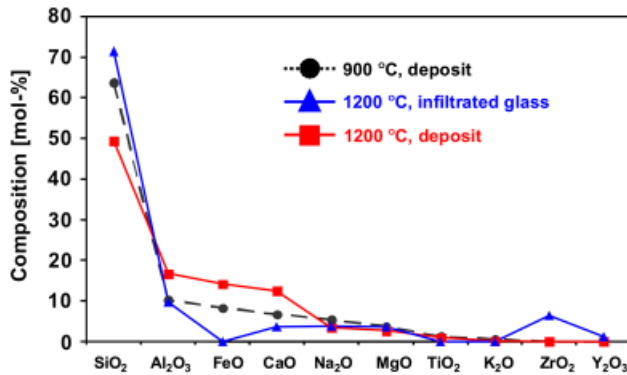


Fig. 12. Compositional variation of major constituents (mol%) of (i) initial artificial volcanic ash (AVA) deposit at 900°C (dot symbols) as compared with (ii) the infiltrated amorphous phase at 1200°C located in the EB-PVD Y₂O₃-stabilized ZrO₂ (YSZ) coating (triangles) and (iii) the residual crystalline AVA deposit at 1200°C remaining at the AVA/EB-PVD YSZ interface (squares).

melt infiltration. The typical solution/precipitation of globular ZrO₂ in contact with CMAS-type melts was not observed in case of AVA after short annealing. On the contrary, the formation of ZrSiO₄ has not been observed in CMAS-type scenarios. This is explained by the AVA environment providing a sufficient saturation of SiO₂. A further important difference to the CMAS scenario is the presence of Fe₂O₃ and TiO₂ that accumulates as Fe₂O₃-rich, hematite-type phase at the surface of the EB-PVD coating. This Fe₂O₃ and TiO₂-rich residual deposit may act as a newly formed reactive interface for subsequent CMAS-type contaminations. The fact that a CMAS-type deposit with significant amounts of Fe₂O₃ and TiO₂ was found on actual engine hardware¹⁰ and complex phase formations were observed also in laboratory¹¹ supports this idea.

IV. Conclusions and Outlook

In a lab-scale approach, sol-gel-derived AVA was used in order to examine the possible effects caused by the ingestion and the subsequent deposition of volcanic ash particles on EB-PVD YSZ-coated high-pressure turbine airfoils. AVA shows a variety of high-temperature interactions with YSZ EB-PVD coatings and YSZ powders. In general, these interactions are quite different to those observed for CMAS-type deposits. Above its glass transition temperature of about 930°C, AVA softens and exhibits viscous flowing. YSZ EB-PVD coatings are wetted completely and partially infiltrated by AVA at 1100°C, which is approximately 100–150°C lower than the onset of infiltration by standard CMAS. At 1200°C, the glaze-type AVA overlay is mostly consumed, producing deeper infiltration into the coating except for a residual deposit with plagioclase- and hematite-type phases. Because AVA acts as effective solvent for Y₂O₃ above 1000°C, the Y₂O₃ content in YSZ decreases. A complete destabilization of YSZ, i.e. a phase transformation to monoclinic ZrO₂, was not observed; instead, ZrSiO₄ appears at 1200°C. With respect to phase stability, the short-term exposure of YSZ coatings to a limited amount of AVA did not impose severe thermochemical degradation. The situation may worsen if a much higher amount of AVA is deposited and a long-term thermal load is applied. Additionally, detrimental effects not investigated in the present work may occur. It is anticipated that an infiltrated YSZ EB-PVD coating will suffer higher thermal

stresses on thermal cycling and consequently resulting in a lower lifetime. Additionally, the TBC functionality will probably be affected by microstructural effects such as pore filling and pore coalescence, i.e. thermal insulation performance may gradually deteriorate as observed for the CMAS scenario.¹⁹ Moreover, a thermochemical interaction of infiltrated AVA and the thermally grown oxide layer located at the YSZ/bondcoat interface of in-service airfoils cannot be ruled out. The relative low softening temperature and the viscous flow behavior of AVA may also cause severe problems in airfoil areas exhibiting cooling boreholes. It must be emphasized that ashes from different volcanic provinces exhibit different chemical and phase compositions and hence will interact with 4YSZ TBC in a case-specific manner. This makes it difficult to derive a general statement about the impact of volcanic ashes on TBC performance. Additional work is required in order to further address these open issues.

References

- N. P. Padture, M. Gell, and E. H. Jordan, "Thermal Barrier Coatings for Gas-Turbine Engine Applications," *Science*, **296**, 280–4 (2002).
- J. L. Smialek, F. A. Archer, and R. G. Garlick, "The Chemistry of Saudi Arabian Sand: A Deposition Problem on Helicopter Turbine Airfoils"; pp. M63–M77 in *Advances in Synthesis and Processes, 3rd International SAMPE Metals Conference*, Edited by F. H. Froes. Society for the Advancement of Material and Process Engineering, Covina, CA, 1992.
- F. H. Stott, D. J. de Wet, and R. Taylor, "The Effect of Molten Silicate Deposits on the Stability of Thermal Barrier Coatings for Turbine Applications at Very High Temperatures"; pp. M92–M101 in *Advances in Synthesis and Processes, 3rd International SAMPE Metals Conference*, Edited by F. H. Froes. Society for the Advancement of Material and Process Engineering, Covina, CA, 1992.
- J. Kim, M. G. Dunn, A. J. Baran, D. P. Wade, and E. L. Tremba, "Deposition of Volcanic Materials in the Hot Sections of Two Gas Turbine Engines," *J. Eng. Gas Turbines Power*, **115** [3] 641–51 (1993).
- D. J. de Wet, R. Taylor, and F. H. Stott, "Corrosion Mechanisms of ZrO₂-Y₂O₃ Thermal Barrier Coatings in the Presence of Molten Middle-East Sand," *J. Phys. IV*, **3** [C9] 655–63 (1993).
- F. H. Stott, D. J. de Wet, and R. Taylor, "Degradation of Thermal-Barrier Coatings at Very High Temperatures," *MRS Bull.*, **19** [10] 46–9 (1994).
- J. L. Smialek, F. A. Archer, and R. G. Garlick, "Turbine Airfoil Degradation in the Persian Gulf War," *J. Min. Metal. Mater. Soc.*, **46** [12] 39–41 (1994).
- S. Krämer, J. Yang, C. G. Levi, and C. A. J. Johnson, "Thermochemical Interaction of Thermal Barrier Coatings with Molten CaO-MgO-Al₂O₃-SiO₂ (CMAS) Deposits," *J. Am. Ceram. Soc.*, **89** [10] 3167–75 (2006).
- K. M. Grant, S. Krämer, J. P. A. Löfvander, and C. G. Levi, "CMAS Degradation of Environmental Barrier Coatings," *Surf. Coat. Technol.*, **202** [4–7] 653–7 (2007).
- W. Braue, "Environmental Stability of the YSZ Layer and the YSZ/TGO Interface of an In-Service EB-PVD Coated High-Pressure Turbine Blade," *J. Mater. Sci.*, **44**, 1664–75 (2009).
- P. Mechnich and W. Braue, "ZrO₂ Environmental Barrier Coatings for Oxide/Oxide Ceramic Matrix Composites Fabricated by Electron-Beam Physical Vapor Deposition"; pp. 285–93 in *Design, Development, and Applications of Engineering Ceramics and Composites*, Edited by D. Singh, D. Zhu, and Y. Zhu. Wiley-Blackwell, Hoboken, NJ, 2010.
- Nordic Volcanological Center, Institute of Earth Science, University of Iceland, Reykjavik, Iceland. Available at <http://www.earthice.hi.is>
- R. W. Le Maitre (ed), *Igneous Rocks: A Classification and Glossary of Terms*. Cambridge University Press, Cambridge, U.K., 2005.
- I. E. E. Carmichael, F. J. Turner, and J. Verhoogen, *Igneous Petrology*. Mc Graw Hill, NY, 1974.
- Y. Kanno, "Discussion of the Double Oxides Formation in the Systems of ZrO₂-SiO₂, ZrO₂-TiO₂ and TiO₂-SiO₂," *J. Mater. Sci. Lett.*, **9**, 765–7 (1990).
- D. R. Spearing and J. Y. Huang, "Zircon Synthesis Via Sintering of Milled SiO₂ and ZrO₂," *J. Am. Ceram. Soc.*, **81** [7] 1964–6 (1998).
- G. Teufer, "Crystal Structure of Tetragonal ZrO₂," *Acta Crystallogr.*, **15** [11] 1187 (1962).
- R. P. Ingel and D. Lewis III, "Lattice Parameters and Density for Y₂O₃-Stabilized ZrO₂," *J. Am. Ceram. Soc.*, **69** [4] 325–32 (1986).
- M. Peters, B. Saruhan-Brings, and U. Schulz, "Advanced Coatings for Blades of Future Aero Engines"; pp. 26–9, *Proceedings of the European Air and Space Conference (CEAS)*, October 26–29, Manchester, U.K., 2009. □